ACS APPLIED MATERIALS & INTERFACES

Research Article

Cite This: ACS Appl. Mater. Interfaces 2018, 10, 36058−36066

www.acsami.org

TiO_2-Nanocoated Black Phosphorus Electrodes with Improved Electrochemical Performance

Yufeng Luo,[†,‡] Hengcai Wu,[†] Liang Liu,[†] Qunqing Li,[†,§] Kaili Jiang,[†,§] Shoushan Fan,[†,‡] Ju Li,[∥] and Jiaping Wang*[,†,§,∥]

[†]Department of Physics and Tsinghua-Foxconn Nanotechnology Research Center and [‡]School of Materials Science and Engineering, Tsinghua University, Beijing 100084, China

[§]Collaborative Innovation Center of Quantum Matter, Beijing 100084, China

[∥]Department of Nuclear Science and Engineering and Department of Materials Science and Engineering, Massachusetts Institute of Technology, Cambridge, Massachusetts 02139, United States

Supporting Information

ABSTRACT: Black phosphorus (BP) is a promising electrode material with high energy density for lithium-ion batteries. However, volumetric expansion of BP upon lithiation leads to rapid capacity fading of the electrode. Herein, BP composite electrodes are prepared by mixing microsized BP particles with carbon nanotubes and KetjenBlack as dual conducting agents, which facilitate the construction of stable and conductive networks in the electrodes. An ultrathin TiO_2 nanocoating is deposited on the surface of the BP composite electrode by electron-beam evaporation. The TiO_2 nanocoating acts as a protective layer to prevent the BP particles from directly contacting the electrolyte by forming a $Li_xTi_yO_z$ passivation coating on the electrode surface. The $Li_xTi_yO_z$ passivation layer suppresses propagation of the formed irreversible solid electrolyte interlayer on the BP particles, resulting in an improved Coulombic efficiency of the BP electrode. Moreover, the $Li_xTi_yO_z$ passivation layer facilitates lithium-ion diffusion and electron transfer and thus superior cycling and rate performance of the BP electrode are achieved.

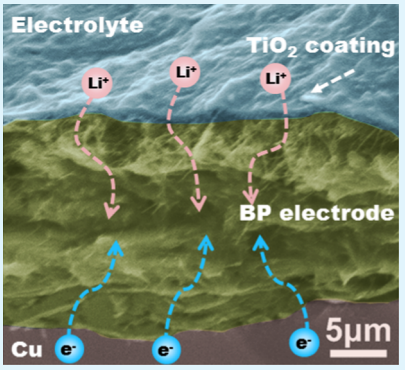

KEYWORDS: *black phosphorus, TiO_2 nanocoating, dual conducting agents, lithium-ion battery, vacuum evaporation*

1. INTRODUCTION

With the rapid development of electric vehicles, new electrode materials with high energy densities are in high demand. Phosphorus is a promising candidate to replace graphite as a new-generation anode material because it possesses high theoretical specific capacity (2596 mAh g^{-1}) and a suitable lithiation potential, which can effectively prevent the formation of metallic lithium plating.[1−6] Among the allotropes of phosphorus, black phosphorus (BP) is more stable than white phosphorus at room temperature and in air, and is more conductive than red phosphorus. BP has attracted widespread attention in a variety of fields, especially for energy storage.[7−15] As a typical two-dimensional material, orthorhombic BP exhibits a honeycomb-puckered structure with a large gap of approximately 0.5 nm between two adjacent phosphorene layers, and lithium ions can rapidly diffuse on the phosphorene layer and inside the bulk BP along the zigzag direction.[16−18] Thus, a potentially excellent rate performance is expected compared to that of the commercial silicon/carbon composites anodes. Therefore, both high energy density and power density can be achieved in BP electrodes for lithium-ion batteries (LIBs). However, similar to Si, Sn, and SnO_2, BP suffers from rapid capacity fading owing to its severe volume change (~300%) as it reacts with three Li atoms to form the Li_3P phase during cycling.[19−21] One approach to solve this issue is to reduce the size of the BP particles. Because of the harsh conditions of BP synthesis and its insolubility in most solvents, it is difficult to reduce the particle size of BP and fabricate BP−carbon composites by simple heat treatment or a solution method.[4,22−25] Recent studies have demonstrated that the cycle life of BP electrodes can be prolonged by reducing the particle size to the nanometer scale by high-energy ball milling or exfoliating BP into a few layers by liquid exfoliation methods.[7−12] Nevertheless, the preparation processes need to be strictly performed in an inert atmosphere owing to the instability of monolayer or few-layer BP in air. Furthermore, the final lithiation product, Li_3P, is insulating and electrochemically inactive,[26] so a large number of carbonaceous materials (usually more than 50 wt %) are added to the BP electrode as a conducting agent, which severely hinders its practical application.

Another reason for the capacity loss of BP anodes is the propagation of the solid electrolyte interlayer (SEI) resulting from severe pulverization of BP particles during cycling. To

Received: August 25, 2018
Accepted: September 27, 2018
Published: September 27, 2018

DOI: 10.1021/acsami.8b14703
ACS Appl. Mater. Interfaces 2018, 10, 36058−36066

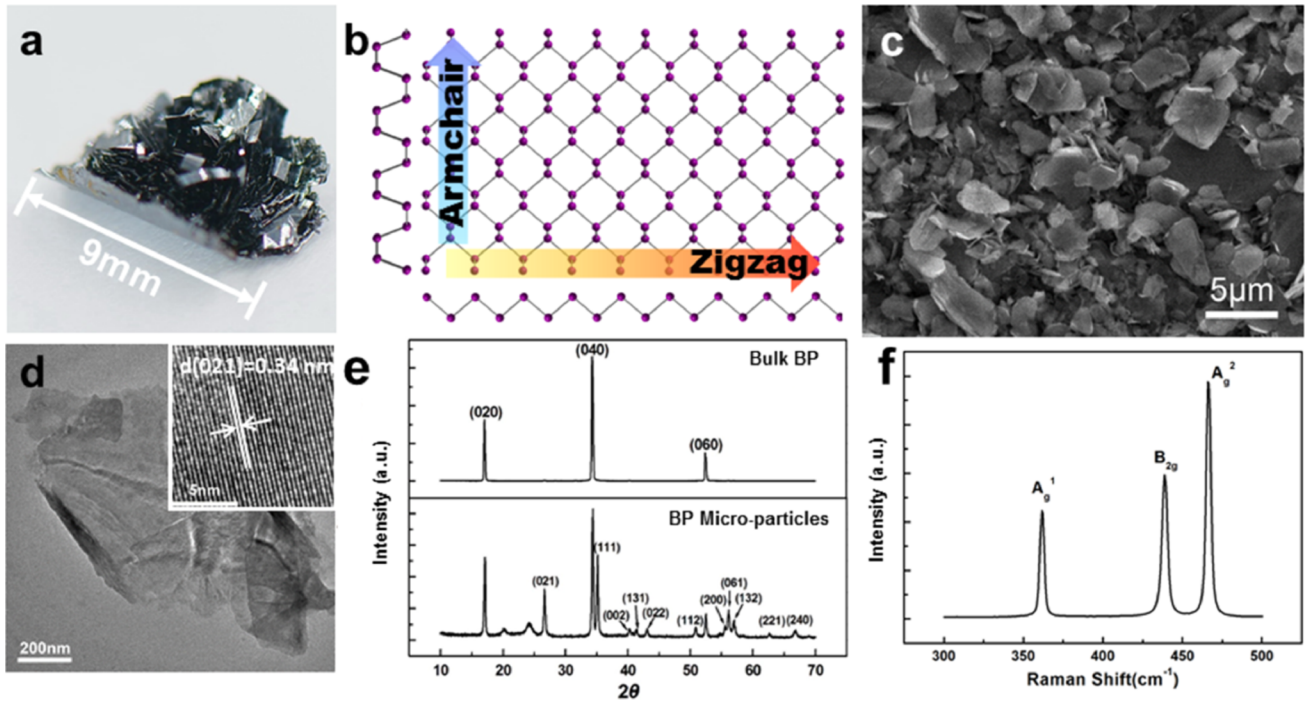

Figure 1. (a) Photograph of a bulk BP single crystal. (b) Top and side views of the atomic structure of phosphorene. (c) SEM image of BP microparticles. (d) TEM image of few-layer phosphorene. (e) XRD patterns of the bulk BP and BP microparticles. (f) Raman spectrum of BP flakes.

address this issue, applying a surface coating to electrodes has been extensively used to provide an interface between the electrode and the electrolyte.[27,28] Differing from the traditional powder-coating approach, the electrode-coating method can protect the surface of the active material from electrolyte erosion while maintaining the electronic pathways between the active material and conductive agents/the current collector in the electrode.[29,30] TiO_2 is considered to be a stable coating material owing to the "zero-strain" characteristics during the formation of Li_xTiO_2 upon lithiation. Especially for amorphous TiO_2 and for small anatase particles, the lithiated Li_xTiO_2 becomes an electronic conductor when x is close to 1.[31,32] Therefore, the TiO_2 coating can tightly adhere to the BP electrode during charge−discharge processes while being beneficial for the electrochemical performance of the electrode. Among a variety of deposition methods, such as layer-by-layer deposition,[33] sputtering,[30] chemical vapor deposition,[34] atomic layer deposition,[29] and vacuum evaporation,[35] the vacuum evaporation method is widely used due to its universality and low cost.

Herein, we fabricated BP electrodes by coating slurries of ball-milled BP particles, carbon nanotube (CNT) and KetjenBlack (KJB) conducting agents, and poly(vinyl difluoride) (PVDF) in *N*-methyl-2-pyrrolidine (NMP) onto Cu current collectors. The content of the microsized BP particles in the electrodes is about 62 wt %. Even though BP is highly conductive, the final lithiation product, Li_3P, is insulating. Therefore, both CNTs and KJB were used as dual conductive agents. Owing to the large aspect ratio of CNTs and excellent electrical conductivities of both CNTs and KJB, a conductive network is established in the electrode that helped to maintain the stable structure of the electrode. An ultrathin TiO_2 coating (thickness of 50 nm) was deposited on the BP electrode by a vacuum evaporation method. The TiO_2 nanocoating acts as a sacrifice layer and provides a stable $Li_xTi_yO_z$ interface between the active material and the electrolyte for suppressing propagation of the in situ formed SEI layer on the BP particles during cycling. Moreover, the $Li_xTi_yO_z$ passivation layer facilitates lithium-ion diffusion and electron transfer, so that the BP electrode with the TiO_2 nanocoating has a specific capacity of 1048 mAh g^{-1} and a Coulombic efficiency of about 99% after 100 cycles, compared with only 706 mAh g^{-1} for the pristine BP electrode.

2. MATERIALS AND METHODS

2.1. Synthesis of BP. Red phosphorus (112 mg), Sn (9 mg), and SnI_4 (4.5 mg) were loaded in a silica ampoule under a vacuum of ∼3 Pa. The ampoule was heated at 400 °C for 2 h, 600 °C for 24 h, and 500 °C for 3 h. The obtained bulk BP sample was ground into a powder, washed with dimethylbenzene at 110 °C to remove any residual mineralizer, and then washed with ethanol. Subsequently, 50 mg of the BP powder was dispersed in 200 mL of NMP by tip sonication (190 W) for 8 h. The BP dispersion was centrifuged at 12 000 rpm for 20 min. The precipitate was washed with ethanol and dried to obtain BP microparticles. Few-layer BP sheets were also collected from the supernatant for structural characterization.

2.2. Preparation of the BP and BP@TiO_2 Electrodes. BP, KJB (600J, SCM Hypnergy Material Tech Co., Ltd., Shanghai, China), CNTs (Beijing Funate Innovation Technology Ltd., Beijing, China), and PVDF were mixed in NMP at a mass ratio of 8:1:1:1. The BP slurry was then ball-milled for 8 h under an argon atmosphere. The ball-milled BP slurry was deposited on a copper foil, dried in a vacuum oven, and cut into 10 mm-diameter pieces to obtain BP electrodes. The typical BP loading was 0.5 mg cm^{-2}. The BP content in the electrode was about 62 wt % based on the thermogravimetric analysis (TGA) results (Figure S1) owing to the loss of BP during the ball-milling process. The BP@TiO_2 electrodes were prepared by coating an ultrathin TiO_2 layer on the BP electrodes in an electron-beam evaporation system (L-400EK, Anelva, Japan) with an evaporation rate of 1 Å s^{-1} under a vacuum of 5×10^{-4} Pa.

DOI: 10.1021/acsami.8b14703
ACS Appl. Mater. Interfaces 2018, 10, 36058−36066

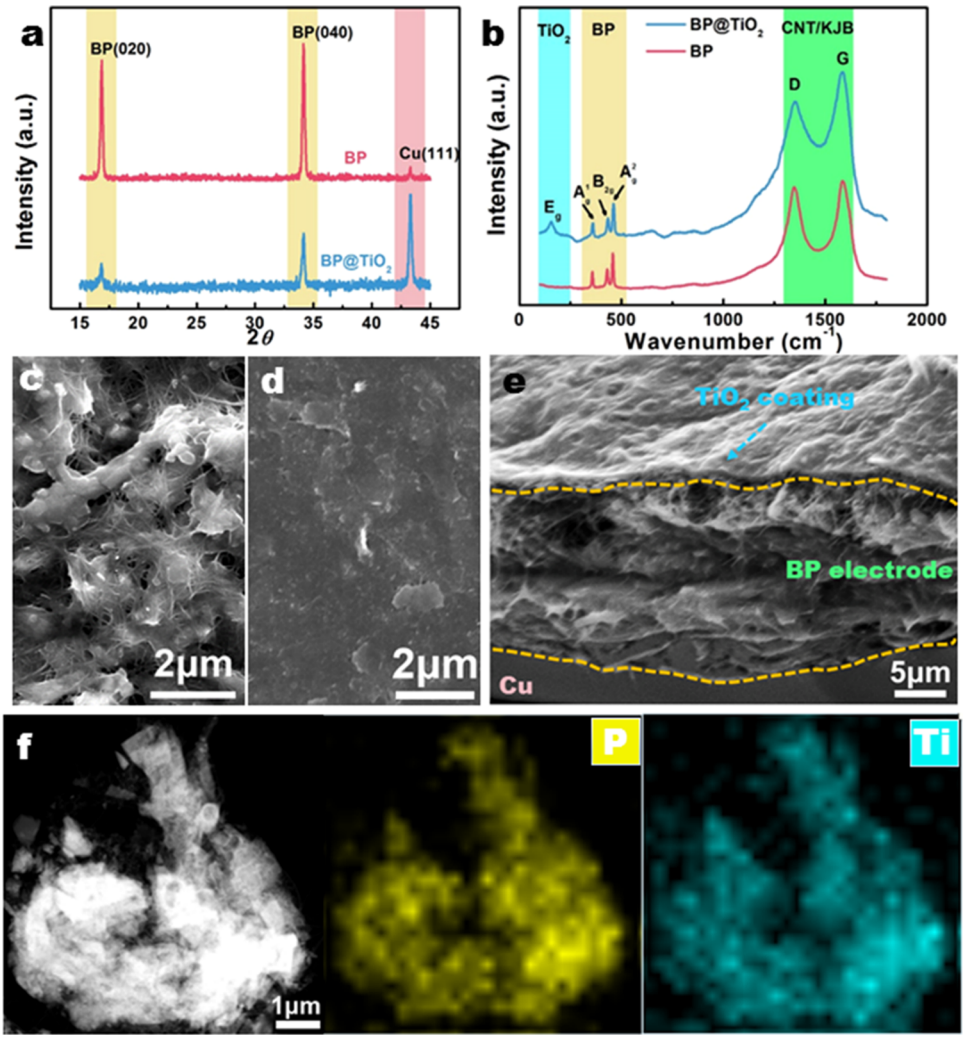

Figure 2. (a) XRD patterns and (b) Raman spectra of the BP and BP@TiO_2 electrodes. SEM images of the surface of the (c) BP and (d) BP@TiO_2 electrodes. (e) Cross section of the BP@TiO_2 electrode. (f) STEM image and its corresponding elemental maps of the BP@TiO_2 electrode.

2.3. Characterization. The structures and morphologies of the BP particles, KJB conducting agent, TiO_2 coating, and electrodes were characterized by X-ray diffraction (XRD), TGA, scanning electron microscopy (SEM), transmission electron microscopy (TEM), energy-dispersive X-ray spectroscopy mapping, X-ray photoelectron spectroscopy (XPS), and Raman spectroscopy. The electrochemical performances of the BP and BP@TiO_2 electrodes were characterized. Experimental details can be found in previous papers.[36,37]

3. RESULTS AND DISCUSSION

Roselike bulk BP single crystals as large as 9 mm composed of submillimeter BP flakes were synthesized by a simple mineralizer-assisted method (Figure 1a). A typical BP crystal consists of atomic BP layers stacked by van der Waals forces (Figure 1b). Each phosphorus atom is covalently bonded to three neighboring phosphorus atoms by sp^3 hybridization, forming a puckered structure. An SEM image of the BP microparticles and a high-resolution TEM (HRTEM) image of few-layer BP are shown in Figure 1c,d. The average size of the BP microparticles is ~5 μm. The lattice fringe of 0.34 nm is indexed to the (021) plane of highly crystalline BP. The XRD patterns of the bulk BP and BP microparticles are shown in Figure 1e. There are three intense diffraction peaks at 17.3, 34.5, and 52.5°, corresponding to the (020), (040), and (060) planes of BP (PDF no. 47-1626). Notably, the BP microparticles that were obtained by mechanical grinding show more diffraction peaks in the XRD pattern, suggesting less preferential orientation compared to that of the bulk BP. The Raman spectrum of the BP flakes in Figure 1f shows three prominent peaks: the out-of-plane phonon mode at 361.6 cm^{-1} (A_g^1) and two in-plane modes at 438.9 cm^{-1} (B_{2g}) and 466.1 cm^{-1} (A_g^2). All of these results suggest high purity and crystallinity of BP with an orthorhombic structure. The microstructure and length distribution of the CNTs and the microstructure and BET results of KJB are shown in Figure S2. The diameter of the CNTs is about 20 nm, and their lengths range from 100 to 1500 nm with an average length of 750 nm. The specific surface area of the KJB conducting agent is about 1344 $m^2\ g^{-1}$ with typical pore sizes of 3 and 10 nm.

A TiO_2 nanocoating was deposited on the surface of the BP electrode by electron-beam evaporation to improve its electrochemical performance. The XRD patterns of the BP and BP@TiO_2 electrodes are shown in Figure 2a. The peaks are indexed to the orthorhombic BP and cubic copper phases. The SEM image of the BP electrode in Figure 2c shows that BP microparticles transformed into microsheets during the ball-milling process. Because of the preferential orientation of the BP microsheets, there are only three main peaks in the XRD pattern. In addition, for the BP@TiO_2 electrode, the

DOI: 10.1021/acsami.8b14703
ACS Appl. Mater. Interfaces 2018, 10, 36058−36066

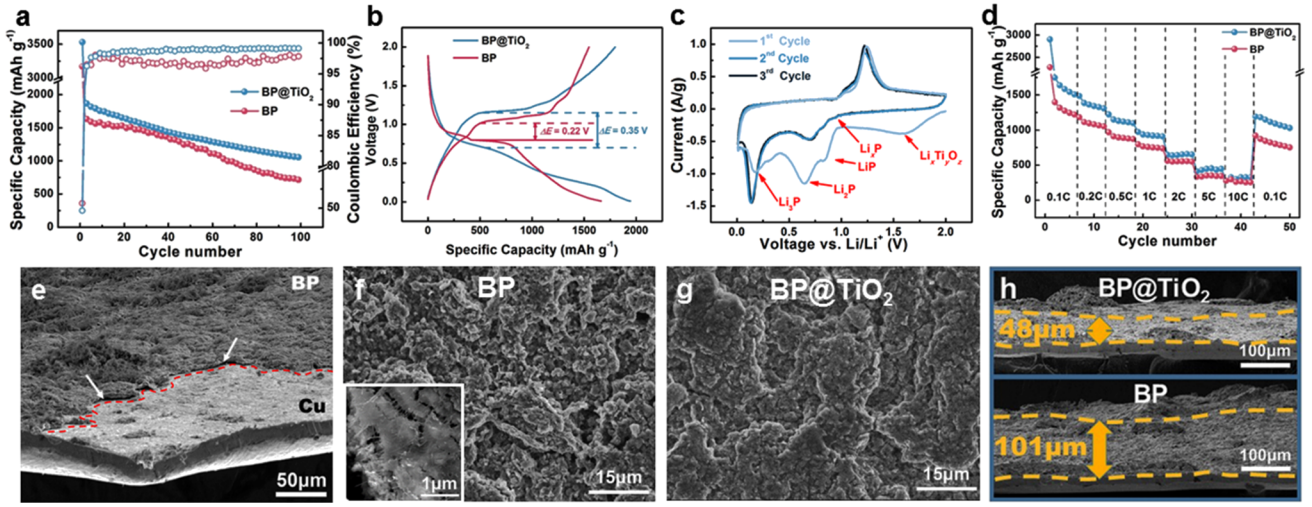

Figure 3. (a) Cycling performance and (b) charge−discharge curves (2nd cycle) of the BP and BP@TiO_2 electrodes. (c) Cyclic voltammetry (CV) curves of the BP@TiO_2 electrode at a scanning rate of 0.1 mV s^{-1}. (d) Rate performance of the BP and BP@TiO_2 electrodes. (e) SEM image of the BP electrode after 30 cycles. (f, g) Surfaces and (h) cross sections of the BP and BP@TiO_2 electrodes after 100 cycles.

peaks of the TiO_2 phase are not observed, indicating the amorphous and ultrathin nature of the TiO_2 nanocoating. Raman spectra of the BP and BP@TiO_2 electrodes are shown in Figure 2b. The Raman peaks at 358, 432, and 462 cm^{-1} correspond to the modes of BP, and the peaks at 1348 and 1582 cm^{-1} are indexed to the carbonaceous conducting agent. The additional peak at 155 cm^{-1} can be attributed to extension vibration of TiO_2 with the anatase structure (E_g mode), and the blue shift of 144 cm^{-1} might result from the reduced grain size and surface strain.[38] The SEM image of the BP electrode shows that the CNT conducting agent is tightly wrapped around the BP microsheets with preferential orientation. As a long-range conducting agent, the CNTs provide continuous conductive paths to bridge different BP microsheets owing to the high aspect ratio of CNTs. As a short-range conducting agent, KJB provides sufficient conductive paths between adjacent BP microsheets owing to its high specific surface area (Figure 2c). For the BP@TiO_2 electrode, a continuous 50 nm-thick TiO_2 layer completely covers the electrode surface (Figure 2d,e). A scanning transmission electron microscope (STEM) image of the BP@TiO_2 electrode and the corresponding EDX maps of P and Ti suggest a uniform TiO_2 nanocoating on the surface of the BP electrode (Figure 2f).

Both the cycling and rate performance of the BP electrode are effectively improved by depositing a TiO_2 nanocoating on the surface of the electrode. The cycling performance of the BP and BP@TiO_2 electrodes at a current density of 0.2C is shown in Figure 3a. The specific capacity of the BP electrode during the 20th cycle is 1496 mAh g^{-1}, and it then rapidly decays. In the 100th cycle, the specific capacity is only 706 mAh g^{-1} and the Coulombic efficiency is 97.85%, with a capacity retention of 41.83% compared to the value in the 2nd cycle, probably because of the microstructure degradation of the electrode. Compared to abnormal attenuation of the BP electrode, both the capacity retention and Coulombic efficiency improve with a TiO_2 nanocoating on the electrode. In the 100th cycle, the specific capacity and Coulombic efficiency of the BP@TiO_2 electrode are 1049 mAh g^{-1} and 99.06%, respectively, with a capacity retention of 53.96%. To evaluate the contribution of TiO_2 to the capacity of the electrode, the cycling performance of the TiO_2 nanocoating was also tested (Figure S3a). In this case, TiO_2 was directly deposited on the Cu foil under the same evaporation condition, with an average mass loading of 0.08 mg cm^{-2}. The initial specific capacity is about 231.8 mAh g^{-1}, and it quickly becomes stable at around 50 mAh g^{-1}, suggesting small contribution of the TiO_2 nanocoating to the overall capacity.

The typical charge−discharge curves and the corresponding voltage hysteresis (ΔE), which are related to the electrochemical reversibility, are also shown in Figure 3b. The BP@TiO_2 anode shows larger capacity but lower discharge plateau and higher charge plateau. The larger voltage gap of 0.35 V suggested that electrode polarization resulted from the TiO_2 nanocoating. After 100 cycles, the voltage hysteresis of the BP@TiO_2 anode reduced to 0.21 V (Figure S4), which benefited from the existence of the TiO_2 nanocoating. In comparison, the voltage hysteresis of the BP anode increased from 0.22 to 0.28 V after 100 cycles. To investigate the lithiation and delithiation processes of the BP and BP@TiO_2 electrodes, the CV profiles of the two electrodes at a scanning rate of 0.1 mV s^{-1} were recorded in the voltage range 0.01−2.0 V (Figure 3c). The broad cathodic peak at 1.65 V may correspond to the lithiation of the anatase TiO_2 nanocoating,[39] and it disappears in the subsequent scans, indicating the irreversibility of the TiO_2 nanocoating. These results could be proved by the charge−discharge curves of the TiO_2 nanocoating (Figure S3b). Besides, the four distinct cathodic peaks and three anodic peaks, belonging to BP, at about 0.93, 0.82, 0.69, and 0.10 V correspond to the formation of Li_xP ($x < 1$), LiP, Li_2P, and Li_3P, respectively.[16,21] The anodic peaks at 1.04, 1.21, and 1.33 V suggest a stepwise delithiation process from the Li_3P phase to the Li_xP phase ($1 \leq x \leq 3$).

The rate performance of the BP and BP@TiO_2 electrodes is shown in Figure 3d. For the BP@TiO_2 electrode, a high reversible capacity of 1508 mAh g^{-1} is obtained at 0.1C during the 6th cycle. As the cycling rate successively increases, the BP@TiO_2 electrode delivers specific capacities of 1308, 1099, 909, 652, 446, and 327 mAh g^{-1} at 0.2, 0.5, 1, 2, 5, and 10C. When the cycling rate sets back to 0.1C, the capacity of the BP@TiO_2 electrode recovers to 1194 mAh g^{-1}, demonstrating the excellent reversibility of the BP@TiO_2 electrode. For

DOI: 10.1021/acsami.8b14703
ACS Appl. Mater. Interfaces 2018, 10, 36058−36066

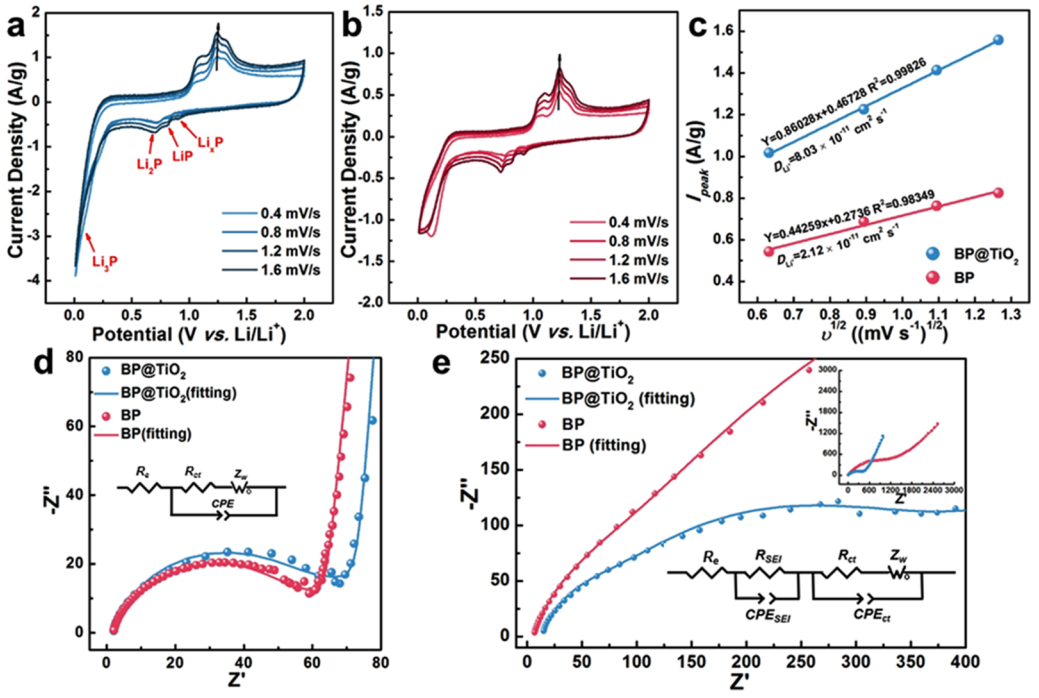

Figure 4. CV curves of the (a) BP and (b) BP@TiO_2 electrodes at scan rates of 0.4, 0.8, 1.2, and 1.6 mV s^{-1}. (c) I_p−$v^{1/2}$ curves of the BP and BP@TiO_2 electrodes. Nyquist plots of the BP and BP@TiO_2 electrodes (d) as fresh cells and (e) after 100 cycles.

comparison, the BP electrode has relatively low specific capacities of 1222, 1053, 870, 739, 550, 344, and 253 mAh g^{-1} at 0.1, 0.2, 0.5, 1, 2, 5, and 10C. Compared with previously reported specific capacities of phosphorus-based anodes at around 0.2C based on the mass of the electrode, the BP@TiO_2 electrode in this work has excellent electrochemical properties at a high phosphorus loading at 62 wt % (Figure S5).[1,4,8,11,12,16,40−42]

Both the BP and BP@TiO_2 electrodes were disassembled after cycling, and their morphologies were characterized to investigate the effect of the TiO_2 nanocoating. The original thickness of the fresh BP electrode was around 10 μm. After 15 and 30 cycles, the thicknesses increased to 12 and 22 μm, respectively, demonstrating the significant volumetric expansion of the BP electrode during cycling (Figure S6). After 30 cycles, there were gaps between the BP electrode and the Cu current collector, as indicated by the arrows in Figure 3e, owing to the volume change, which resulted in the capacity decay of the BP electrode. In contrast, the thickness of the BP@TiO_2 electrode also approximately increased to 12 μm after 15 cycles, which indicated a tiny difference between the two kinds of electrodes in the early cycles. However, after 30 cycles, the thickness of the BP@TiO_2 electrode only slightly increased to 16 μm, suggesting that the TiO_2 nanocoating reduces volume expansion of the BP electrode. The top surfaces and cross sections of the BP and BP@TiO_2 electrodes after 100 cycles are shown in Figure 3f−h. After cycling, the surface of the BP electrode becomes uneven (Figure 3f), which suggests the formation of an amorphous SEI layer. There are some voids and macropores inside the electrode owing to severe volumetric expansion/shrinkage of BP particles. The thickness of the BP electrode increased to 101 μm after 100 cycles. Even though the CNT conducting agent can bridge different parts of the electrode to achieve effective electron transfer among the active materials, which can partly inhibit capacity loss, the collapse of the electrode structure and the detachment of the BP electrode from the current collector owing to volume changes during cycling cause significant capacity decay. In contrast, the surface of the cycled BP@TiO_2 electrode is smoother than that of the BP electrode, and its thickness is only 48 μm after 100 cycles without any apparent voids inside the electrode (Figure 3g,h). According to the SEM results, pulverization of BP also occurs in the BP@TiO_2 electrode. The TiO_2 nanocoating acts as a protective layer, preventing the BP particles from direct contact with the electrolyte, which significantly reduces the generation of an SEI on the BP particles and efficiently inhibits severe capacity decay of the BP@TiO_2 electrode.

The CV measurements were also performed at scanning rates of 0.4, 0.8, 1.2, and 1.6 mV s^{-1} to investigate the lithium diffusion properties (Figure 4a,b). According to the Randles−Sevcik equation

$$I_p = 0.4463nFA\left(\frac{nF}{RT}\right)^{1/2} D^{1/2}v^{1/2}C_{LiPF_6} \quad (1)$$

where I_p is the peak current, n is the number of electrons per reaction species (n = 1), F is Faraday's constant (F = 96485 C mol^{-1}), A is the active electrode area (A = 0.785 cm^2), D is the lithium-ion diffusion coefficient, v is the scanning rate, and C is the lithium-ion concentration (C_{LiPF_6} = 1.0 M). The D values are determined from the slopes of the curves of I_p versus $v^{1/2}$ and related to lithium-ion diffusion.[25,41] As shown in Figure 4c, the slope of the curve for the BP@TiO_2 electrode is 3.8 times higher than that for the BP electrode, resulting in an increase in the Li-ion diffusion coefficient from 2.12 × 10^{-11} to 8.03 × 10^{-11} cm^2 s^{-1} as a result of the TiO_2 nanocoating. The high Li-ion diffusion coefficient for the BP@TiO_2 electrode is beneficial for enhancing the rate capacity of the electrode.

Electrochemical impedance spectroscopy (EIS) was also performed to investigate the lithium-storage performance of the BP and BP@TiO_2 electrodes. As shown in Figure 4d, the

DOI: 10.1021/acsami.8b14703
ACS Appl. Mater. Interfaces 2018, 10, 36058−36066

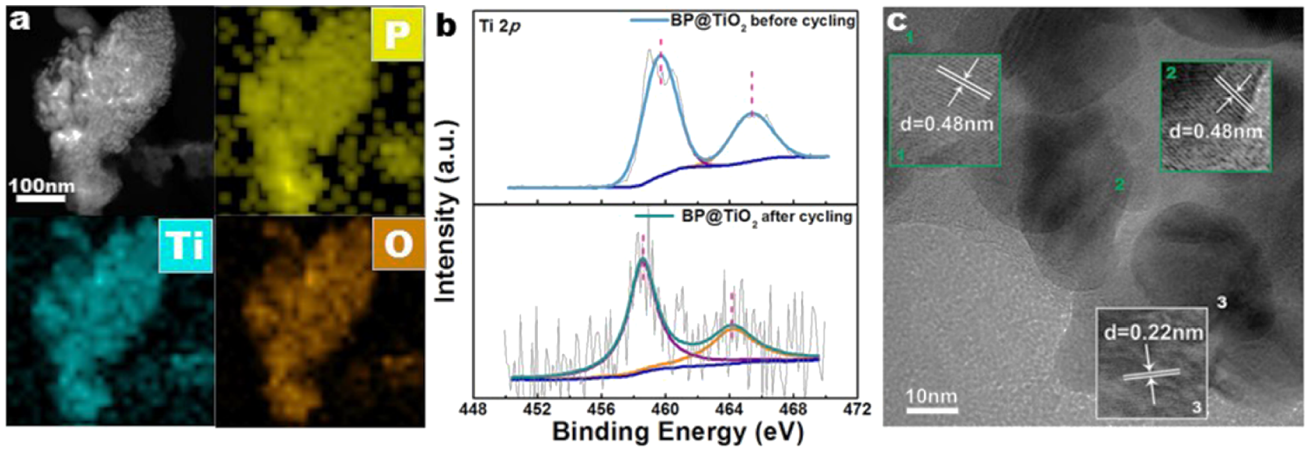

Figure 5. (a) STEM image and the corresponding elemental maps of the BP@TiO_2 electrode after 100 cycles. (b) Ti 2p XPS spectra before and after cycling. (c) HRTEM image of the BP@TiO_2 electrode after 100 cycles. Light zones (1 and 2) represent the $Li_xTi_yO_z$ layer with a lattice spacing of 0.48 nm. Dark zone (3) represents the BP particle with a lattice spacing of 0.22 nm.

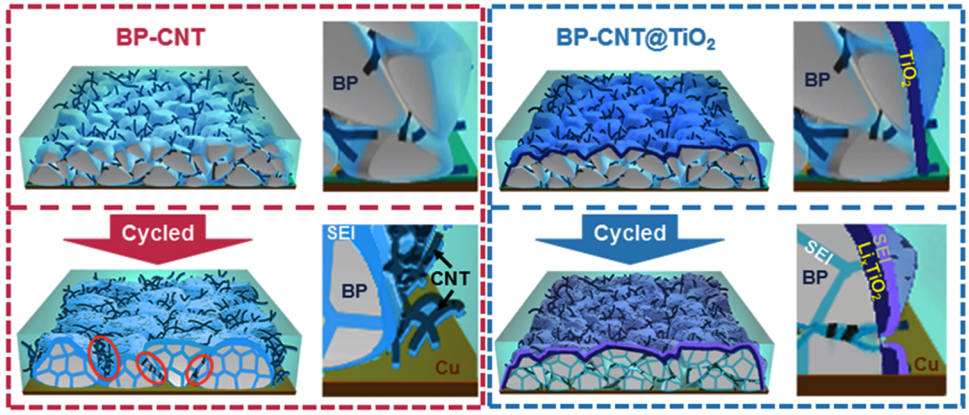

Figure 6. Schematic diagram of the protection mechanism of the TiO_2 sacrificial coating on the BP electrode.

depressed semicircle in the high-frequency region and the inclined line at low frequency represent the charge-transfer resistance (R_{ct}) between the electrolyte and the electrode and the Warburg resistance (W_o) resulting from lithium-ion diffusion inside the electrode material, respectively. According to fitting with the equivalent circuit, the Ohmic resistance (R_s) values of the BP and BP@TiO_2 electrodes are both 1.8 Ω, suggesting similar conditions of the electrolyte resistance, current collectors, and cell connections in these electrodes. The low-frequency slope angle is about 83° for both electrodes. The BP@TiO_2 electrode has a little higher R_{ct} value (58.6 Ω) than that of the BP electrode (52.6 Ω) due to the existence of the TiO_2 nanocoating as fresh cells. These fitting results indicate that the TiO_2 nanocoating stabilizes the interface between the electrolyte and the electrode but does not change the electrode structure. Therefore, lithium-ion diffusion in the electrode is not affected. After 100 cycles, there is an additional semicircle in the high-frequency region (Figure 4e), which can be attributed to the formation of a SEI.[44] The SEI resistance (R_{SEI}) and R_{ct} values of the BP@TiO_2 electrode are 62.3 and 258.2 Ω, respectively, compared with 87.66 and 492.4 Ω for the BP electrode. The low-frequency slope angles of the BP and BP@TiO_2 electrodes decrease to 45 and 65°, respectively, suggesting slower Li-ion diffusion. These results indicate that the structures of both the BP and BP@TiO_2 electrodes undergo degradation during cycling. However, the larger R_{SEI} and R_{ct} values indicated the severer degradation of the BP electrode due to the pulverization of the BP particles and the irreversible SEI. For the BP@TiO_2 electrode, the TiO_2 nanocoating provides a stable interface and suppresses propagation of the in situ formed irreversible SEI on the BP particles to a certain extent.

STEM and EDX were performed to further investigate the protection mechanism of the TiO_2 nanocoating. The STEM image and the corresponding EDX maps of the BP@TiO_2 electrode after 100 cycles in Figure 5a show a uniform distribution of P, Ti, and O elements, suggesting an intact TiO_2 layer on the surface of the electrode after cycling. XPS was performed to identify the Ti states in the BP@TiO_2 electrode before and after cycling (Figure 5b). For the fresh TiO_2 nanocoating, the spin-energy separation is about 5.7 eV, indicating the dominance of the Ti^{4+} oxidation state. After cycling, the intensities of the TiO_2 peaks become weak, and the peaks shift to lower binding energy by ∼1 eV. The shifts might be due to the transformation from Ti^{4+} to Ti^{3+} and formation of $Li_xTi_yO_z$.[31] The HRTEM image in Figure 5c shows crystalline $Li_xTi_yO_z$ and BP nanoparticles. The lattice spacing of 0.48 nm in the light zone corresponds to the $Li_xTi_yO_z$ layer (Table S1), and the lattice spacing of 0.22 nm in the dark zone is ascribed to the (041) plane of the BP particles. The particle sizes of BP decrease from micrometers to nanometers owing to pulverization during cycling, and a $Li_xTi_yO_z$ layer forms on the

DOI: 10.1021/acsami.8b14703
ACS Appl. Mater. Interfaces 2018, 10, 36058−36066

surface of the BP particles. According to the EIS results, the BP@TiO_2 electrode has a lower R_{ct} value than that of the BP electrode, suggesting suppressed degradation of the electrode structure. It can be inferred that the $Li_xTi_yO_z$ coating formed on the BP particles acts as a stable and inert layer between the electrolyte and the surface of the BP electrode. The $Li_xTi_yO_z$ coating efficiently minimizes the formation of the SEI on the BP electrode, and its electrochemical performance significantly improves.[43,45]

To study the effect of TiO_2 nanocoating on the BP electrode, both BP and BP@TiO_2 electrodes exposed to ambient conditions for 10 days were also tested as anodes (Figure S7). The exposed BP@TiO_2 electrode still exhibited high specific capacity of 982 mAh g^{-1} after 100 cycles at 0.2C compared to the as-prepared BP@TiO_2 electrode (1049 mAh g^{-1}). For the BP electrode (706 mAh g^{-1}), the specific capacity maintained at only 458 mAh g^{-1} after 10 days of exposure, which suggested the slight degradation of BP electrode after depositing the TiO_2 nanocoating.

The protection mechanism of the TiO_2 nanocoating as a sacrifice layer is shown in Figure 6. The bare BP electrode is directly exposed to the electrolyte, and a SEI forms on the surface of the BP microparticles. During cycling, the volume change of the BP particles results in severe pulverization and propagation of the SEI, which is confirmed by the increases in the R_{SEI} and R_{ct} values from the EIS measurements. The sizes of the cracks and voids in the electrode gradually increase, which further increases the direct contact area between the BP electrode and the electrolyte. Therefore, the electrode becomes thicker, and its surface becomes more uneven. Even though the CNT conducting agent can link the BP particles to a certain extent, continuous pulverization of the BP particles and formation of voids and the SEI contribute to the capacity decay of the electrode. After nanocoating a TiO_2 sacrifice layer on the BP electrode, both a SEI and a $Li_xTi_yO_z$ layer form on the surface of the BP electrode during cycling. The $Li_xTi_yO_z$ layer effectively inhibits the generation of the SEI on the surface of the BP particles by decreasing the direct contact area between the BP electrode and the electrolyte. Therefore, structural degradation of the electrode is suppressed, and the cycling performance significantly improves. The $Li_xTi_yO_z$ layer also maintains a pathway for ion diffusion and electron transfer, leading to improved rate performance of the electrode.

4. CONCLUSIONS

A protective TiO_2 nanocoating has been directly deposited on the surface of the BP electrode to enhance its electrochemical performance. With two carbonaceous conducting agents, the BP content in the electrode is as high as 62 wt %. The ultrathin TiO_2 nanocoating effectively suppresses the formation of the SEI on the BP electrode and inhibits the structural degradation of the BP electrode during cycling by forming a stable $Li_xTi_yO_z$ layer between the electrolyte and the BP particles. The $Li_xTi_yO_z$ layer enhances ionic conduction at the interface between the electrode and the electrolyte, while maintaining electronic conduction in the electrode. Therefore, the electrochemical performance of the BP electrode was effectively improved. These results demonstrate that depositing a low-cost TiO_2 nanocoating on the electrode surface is a facile approach to improve the performance of BP electrodes, which paves the way for the practical application of BP as the anode material for LIBs.

■ ASSOCIATED CONTENT

Supporting Information

The Supporting Information is available free of charge on the ACS Publications website at DOI: 10.1021/acsami.8b14703.

TGA curve of the BP@TiO_2 electrode; morphologies of CNTs and KJB; charge−discharge curves of the TiO_2, BP, and BP@TiO_2 electrodes; SEM images of the BP and BP@TiO_2 electrodes after cycling; cycling performances of the BP and BP@TiO_2 electrodes after exposure for 10 days; data of the lithiation products of TiO_2 (PDF)

■ AUTHOR INFORMATION

Corresponding Author

*E-mail: jpwang@tsinghua.edu.cn.

ORCID

Yufeng Luo: 0000-0002-5121-8718
Qunqing Li: 0000-0001-9565-0855
Ju Li: 0000-0002-7841-8058
Jiaping Wang: 0000-0002-8300-4992

Notes

The authors declare no competing financial interest.

■ ACKNOWLEDGMENTS

J.W. acknowledges support by NSFC (No. 51472141). Q.L. acknowledges support by the National Key Research and Development Program of China (No. 2017YFA0205800). J.L. acknowledges support by NSF ECCS-1610806.

■ REFERENCES

(1) Yu, Z.; Song, J.; Gordin, M. L.; Yi, R.; Tang, D. H. Phosphorus-Graphene Nanosheet Hybrids as Lithium-Ion Anode with Exceptional High-Temperature Cycling Stability. *Adv. Sci.* **2015**, *2*, No. 1400020, DOI: 10.1002/advs.201400020.

(2) Wang, Y. L.; Tian, L. Y.; Yao, Z. H.; Li, F.; Li, S.; Ye, S. H. Enhanced Reversibility of Red Phosphorus/Active Carbon Composite as Anode for Lithium Ion Batteires. *Electrochim. Acta* **2015**, *163*, 71−75.

(3) Li, W. H.; Yang, Z. Z.; Jiang, Y.; Yu, Z. R.; Gu, L.; Yu, Y. Crystalline Red Phosphorus Incorporated with Porous Carbon Nanofibers as Flexible Electrode for High Performance Lithium-Ion Batteries. *Carbon* **2014**, *78*, 455−462.

(4) Li, W.; Yang, Z. Z.; Li, M. S.; Jiang, Y.; Wei, X.; Zhong, X. W.; Gu, L.; Yu, Y. Amorphous Red Phosphorus Embedded in Highly Ordered Mesoporous Carbon with Superior Lithium and Sodium Capacity. *Nano Lett.* **2016**, *16*, 1546−1553.

(5) Liu, S.; Feng, J. K.; Bian, X. F.; Liu, J.; Xu, H.; An, Y. L. A Controlled Red Phosphorus @Ni-P Core@Shell Nanostructure as An Ultralong Cycle-Life and Superior High-Rate Anode for Sodium-Ion Batteries. *Energy Environ. Sci.* **2017**, *10*, 1222−1233.

(6) Liu, S.; Xu, H.; Bian, X. F.; Feng, J. K.; Liu, J.; Yang, Y. H.; Yuan, C.; An, Y. L.; Fan, R. H.; Ci, L. J. Nanoporous Red Phosphorus on Reduced Graphene Oxide as Superior Anode for Sodium-Ion Batteries. *ACS Nano* **2018**, *12*, 7380−7387.

(7) Park, C. M.; Sohn, H. J. Black Phosphorus and Its Composite for Lithium Rechargeable Batteries. *Adv. Mater.* **2007**, *19*, 2465−2468.

(8) Sun, J.; Zheng, G. Y.; Lee, H. W.; Liu, N.; Wang, H. T.; Yao, H. B.; Yang, W. S.; Cui, Y. Formation of Stable Phosphorus-Carbon Bond for Enhanced Performance in Black Phosphorus Nanoparticle-Graphite Composite Battery Anodes. *Nano Lett.* **2014**, *14*, 4573−4580.

(9) Dahbi, M.; Yabuuchi, N.; Fukunishi, M.; Kubota, K.; Chihara, K.; Tokiwa, K.; Yu, X. F.; Ushiyama, H.; Yamashita, K.; Son, J. Y.; Cui, Y. T.; Oji, H.; Komaba, S. Black phosphorus as A High-Capacity

DOI: 10.1021/acsami.8b14703
ACS Appl. Mater. Interfaces 2018, 10, 36058−36066

and High-Capability Negative Electrode for Sodium-Ion Batteries: Investigation of the Electrode/Electrolyte Interface. *Chem. Mater.* **2016**, *28*, 1625−1635.
(10) Xu, G. L.; Chen, Z. H.; Zhong, G. M.; Liu, Y. Z.; Yang, Y.; Ma, T. Y.; Ren, Y.; Zuo, X. B.; Wu, X. H.; Zhang, X. Y.; Amine, K. Nanostructured Black Phosphorus/Ketjenblack-Multiwalled Carbon Nanotubes Composite as High Performance Anode Material for Sodium-Ion Batteries. *Nano Lett.* **2016**, *16*, 3955−3965.
(11) Zhang, Y.; Wang, H. W.; Luo, Z. Z.; Tan, H. T.; Li, B.; Sun, S. N.; Li, Z.; Zong, Y.; Xu, Z. C. J.; Yang, Y. H.; Khor, K. A.; Yan, Q. Y. An Air-Stable Densely Packed Phosphorene−Graphene Composite Toward Advanced Lithium Storage Properties. *Adv. Energy Mater.* **2016**, *6*, No. 1600453.
(12) Chen, L.; Zhou, G. M.; Liu, Z. B.; Ma, X. M.; Chen, J.; Zhang, Z. Y.; Ma, X. L.; Li, F.; Cheng, H. M.; Ren, W. C. Scalable Clean Exfoliation of High-Quality Few-Layer Black Phosphorus for a Flexible Lithium Ion Battery. *Adv. Mater.* **2016**, *28*, 510−517.
(13) Liu, Y.; Liu, Q. Z.; Zhang, A. Y.; Cai, J. S.; Cao, X.; Li, Z.; Asimow, P. D.; Zhou, C. W. Room-Temperature Pressure Synthesis of Layered Black Phosphorus-Graphene Composite for Sodium-Ion Battery Anodes. *ACS Nano* **2018**, *12*, 8323−8329.
(14) Qiu, M.; Sun, Z. T.; Sang, D. K.; Han, X. G.; Zhang, H.; Niu, C. M. Current Progress in Black Phosphorus Materials and Their Applications in Electrochemical Energy Storage. *Nanoscale* **2017**, *9*, 13384−13403.
(15) Ni, J. F.; Li, L.; Lu, J. Phosphorus: An Anode of Choice for Sodium-Ion Batteries. *ACS Energy Lett.* **2018**, *3*, 1137−1144.
(16) Liu, H.; Zou, Y. Q.; Tao, L.; Ma, Z. L.; Liu, D. D.; Zhou, P.; Liu, H. B.; Wang, S. Y. Sandwiched Thin-Film Anode of Chemically Bonded Black Phosphorus/Graphene Hybrid for Lithium-Ion Battery. *Small* **2017**, *13*, No. 1700758.
(17) Guo, G. C.; Wei, X. L.; Wang, D.; Luo, Y. P.; Liu, L. M. Pristine and Defect-Containing Phosphorene as Promising Anode Materials for Rechargeable Li Batteries. *J. Mater. Chem. A* **2015**, *3*, 11246−11252.
(18) Zhang, R.; Wu, X. J.; Yang, J. L. Blockage of Ultrafast and Directional Diffusion of Li Atoms on Phosphorene With Intrinsic Defects. *Nanoscale* **2016**, *8*, 4001−4006.
(19) Li, W.; Yang, Y. M.; Zhang, G.; Zhang, Y. W. Ultrafast and Directional Diffusion of Lithium in Phosphorene for High-Performance Lithium-Ion Battery. *Nano Lett.* **2015**, *15*, 1691−1697.
(20) Zhao, S. J.; Kang, W.; Xue, J. M. The Potential Application of Phosphorene as An Anode Material in Li-Ion Batteries. *J. Mater. Chem. A* **2014**, *2*, 19046−19052.
(21) Mayo, M.; Griffith, K. J.; Pickard, C. J.; Morris, A. J. Ab Initio Study of Phosphorus Anodes for Lithium- and Sodium-Ion Batteries. *Chem. Mater.* **2016**, *28*, 2011−2021.
(22) Xia, W. W.; Zhang, Q. B.; Xu, F.; Ma, H. Y.; Chen, J.; Qasim, K.; Ge, B. H.; Zhu, C. Y.; Sun, L. T. Visualizing the Electrochemical Lithiation/Delithiation Behaviors of Black Phosphorus by in Situ Transmission Electron Microscopy. *J. Phys. Chem. C* **2016**, *120*, 5861−5868.
(23) Qian, J.; Qiao, D.; Ai, X. P.; Cao, Y. L.; Yang, H. X. Reversible 3-Li Storage Reactions of Amorphous Phosphorus as High Capacity and Cycling-Stable Anodes for Li-Ion Batteries. *Chem. Commun.* **2012**, *48*, 8931−8933.
(24) Ramireddy, T.; Xing, T.; Rahman, M. M.; Chen, Y.; Dutercq, Q.; Gunzelmann, D.; Glushenkov, A. M. Phosphorus−Carbon Nanocomposite Anodes for Lithium-Ion and Sodium-Ion Batteries. *J. Mater. Chem. A* **2015**, *3*, 5572−5584.
(25) Li, J.; Wang, L.; He, X. M.; Wang, J. L. Effect of Pore Size Distribution of Carbon Matrix on the Performance of Phosphorus@Carbon Material as Anode for Lithium-Ion Batteries. *ACS Sustainable Chem. Eng.* **2016**, *4*, 4217−4223.
(26) Zhao, Z. Y.; Liu, L. L.; Yu, T.; Yang, G. C.; Bergara, A. Pressure-Induced Stable Li_5P for High-Performance Lithium-Ion Batteries. *J. Phys. Chem. C* **2017**, *121*, 21199−21205.
(27) Meng, X.; Yang, X. Q.; Sun, X. L. Emerging Applications of Atomic Layer Deposition for Lithium-Ion Battery Studies. *Adv. Mater.* **2012**, *24*, 3589−3615.
(28) Wang, X.; Yushin, G. Chemical Vapor Deposition and Atomic Layer Deposition for Advanced Lithium Ion Batteries and Supercapacitors. *Energy Environ. Sci.* **2015**, *8*, 1889−1904.
(29) Jung, Y. S.; Cavanagh, A. S.; Riley, L. A.; Kang, S. H.; Dillon, A. C.; Groner, M. D.; George, S. M.; Lee, S. H. Ultrathin Direct Atomic Layer Deposition on Composite Electrodes for Highly Durable and Safe Li-Ion Batteries. *Adv. Mater.* **2010**, *22*, 2172−2176.
(30) Zhou, A.; Dai, X. Y.; Lu, Y. T.; Wang, Q. J.; Fu, M. S.; Li, J. Z. Enhanced Interfacial Kinetics and High-Voltage/High-Rate Performance of $LiCoO_2$ Cathode by Controlled Sputter-Coating with a Nanoscale $Li_4Ti_5O_{12}$ Ionic Conductor. *ACS Appl. Mater. Interfaces* **2016**, *8*, 34123−34131.
(31) Lotfabad, E. M.; Kalisvaart, P.; Cui, K.; Kohandehghan, A.; Kupsta, M.; Olsen, B.; Mitlin, D. ALD TiO_2 Coated Silicon Nanowires for Lithium Ion Battery Anodes with Enhanced Cycling Stability and Coulombic Efficiency. *Phys. Chem. Chem. Phys.* **2013**, *15*, 13646−13657.
(32) Lotfabad, E. M.; Kalisvaart, P.; Kohandehghan, A.; Cui, K.; Kupsta, M.; Farbod, B.; Mitlin, D. Si Nanotubes ALD Coated with TiO_2, TiN or Al_2O_3 as High Performance Lithium Ion Battery Anodes. *J. Mater. Chem. A* **2014**, *2*, 2504−2516.
(33) Ariga, K.; Yamauchi, Y.; Rydzek, G.; Ji, Q.; Yonamine, Y.; Wu, K. C.-W.; Hill, J. P. Layer-By-Layer Nanoarchitectonics: Invention, Innovation, and Evolution. *Chem. Lett.* **2014**, *115*, 1−4.
(34) Cheng, L.; Yan, J.; Zhu, G. N.; Luo, J. Y.; Wang, C. X.; Xia, Y. Y. General Synthesis of Carbon-Coated Nanostructure $Li_4Ti_5O_{12}$ as A High Rate Electrode Material for Li-Ion Intercalation. *J. Mater. Chem.* **2010**, *20*, 595−602.
(35) Nuli, Y. N.; Zhao, S. L.; Qin, Q. Z. Nanocrystalline Tin Oxides and Nickel Oxide Film Anodes for Li-Ion Batteries. *J. Power Sources* **2003**, *114*, 113−120.
(36) Luo, Y. F.; Wang, K.; Luo, S.; Zhao, F.; Wu, H. C.; Jiang, K. L.; Li, Q. Q.; Fan, S. S.; Wang, J. P. Three-Dimensional Carbon Nanotube/Transition-Metal Oxide Sponges as Composite Electrodes with Enhanced Electrochemical Performance. *ACS Appl. Nano Mater.* **2018**, *1*, 2997−3005.
(37) Luo, Y.; Luo, N.; Kong, W. B.; Wu, H. C.; Wang, K.; Fan, S. S.; Duan, W. H.; Wang, J. P. Multifunctional Interlayer Based on Molybdenum Diphosphide Catalyst and Carbon Nanotube Film for Lithium-Sulfur Batteries. *Small* **2018**, No. 1702853.
(38) Xu, C. Y.; Zhang, P. X.; Yan, L. Blue Shift of Raman Peak from Coated TiO_2 Nanoparticles. *J. Raman Spectrosc.* **2001**, *32*, 862−865.
(39) Wang, D.; Choi, D.; Li, J.; Yang, Z. G.; Nie, Z. M.; Kou, R.; Hu, D. H.; Wang, C. M.; Saraf, L. V.; Zhang, J. G.; Aksay, I. A.; Liu, J. Self-Assembled TiO_2-Graphene Hybrid Nanostructures for Enhanced Li-Ion Insertion. *ACS Nano* **2009**, *3*, 907−914.
(40) Gao, H.; Zhou, T. F.; Zheng, Y.; Liu, Y. Q.; Chen, J.; Liu, H. K.; Guo, Z. P. Integrated Carbon/Red Phosphorus/Graphene Aerogel 3D Architecture via Advanced Vapor-Redistribution for High-Energy Sodium-Ion Batteries. *Adv. Energy Mater.* **2016**, *6*, No. 1601037.
(41) Wang, L. Y.; Guo, H. L.; Wang, W.; Teng, K. Y.; Xu, Z. W.; Chen, C.; Li, C. Y.; Yang, C. Y.; Hu, C. S. Preparation of Sandwich-Like Phosphorus/Reduced Graphene Oxide Composites as Anode Materials for Lithium-Ion Batteries. *Electrochim. Acta* **2016**, *211*, 499−506.
(42) Zhang, Y. Y.; Rui, X. H.; Tang, Y. X.; Liu, Y. Q.; Wei, J. Q.; Chen, S.; Leow, W. R.; Li, W. L.; Liu, Y. J.; Deng, J. Y.; Ma, B.; Yan, Q. Y.; Chen, X. D. Wet-Chemical Processing of Phosphorus Composite Nanosheets for High-Rate and High-Capacity Lithium-Ion Batteries. *Adv. Energy Mater.* **2016**, *6*, No. 1502409.
(43) Wang, H. Y.; Wang, F. M. Electrochemical Investigation of An Artificial Solid Electrolyte Interface for Improving the Cycle-Ability of Lithium Ion Batteries Using An Atomic Layer Deposition on A Graphite Electrode. *J. Power Sources* **2013**, *233*, 1−5.
(44) Xu, J. T.; Jeon, I. Y.; Ma, J. M.; Dou, Y. H.; Kim, S. J.; Seo, J. M.; Liu, H. K.; Dou, S. X.; Baek, J. B.; Dai, L. M. Understanding of the

DOI: 10.1021/acsami.8b14703
ACS Appl. Mater. Interfaces 2018, 10, 36058−36066

Capacity Contribution of Carbon in Phosphorus-Carbon Composites for High-Performance Anodes in Lithium Ion Batteries. *Nano Res.* **2017**, *10*, 1268−1281.
(45) Lee, M. L.; Su, C. Y.; Lin, Y. H.; Liao, S. C.; Chen, J. M.; Perng, T. P.; Yeh, J. W.; Shih, H. C. Atomic Layer Deposition of TiO_2 on Negative Electrode for Lithium Ion Batteries. *J. Power Sources* **2013**, *244*, 410−416.

DOI: 10.1021/acsami.8b14703
ACS Appl. Mater. Interfaces 2018, 10, 36058−36066